

# PillarNet: Real-Time and High-Performance Pillar-based 3D Object Detection

Guangsheng Shi<sup>1</sup>, Ruiyuan Li<sup>1</sup>, and Chao Ma<sup>2</sup>

<sup>1</sup> State Key Laboratory of Robotics and System, Harbin Institute of Technology

<sup>2</sup> MoE Key Lab of Artificial Intelligence, AI Institute, Shanghai Jiao Tong University  
`sgsadvance@163.com, lrf100@hit.edu.cn, chaoma@sjtu.edu.cn`

**Abstract.** Real-time and high-performance 3D object detection is of critical importance for autonomous driving. Recent top-performing 3D object detectors mainly rely on point-based or 3D voxel-based convolutions, which are both computationally inefficient for onboard deployment. In contrast, pillar-based methods use solely 2D convolutions, which consume less computation resources, but they lag far behind their voxel-based counterparts in detection accuracy. In this paper, by examining the primary performance gap between pillar- and voxel-based detectors, we develop a real-time and high-performance pillar-based detector, dubbed PillarNet. The proposed PillarNet consists of a powerful encoder network for effective pillar feature learning, a neck network for spatial-semantic feature fusion and the commonly used detect head. Using only 2D convolutions, PillarNet is flexible to an optional pillar size and compatible with classical 2D CNN backbones, such as VGGNet and ResNet. Additionally, PillarNet benefits from our designed orientation-decoupled IoU regression loss along with the IoU-aware prediction branch. Extensive experimental results on large-scale nuScenes Dataset and Waymo Open Dataset demonstrate that the proposed PillarNet performs well over the state-of-the-art 3D detectors in terms of effectiveness and efficiency. The source code is available at <https://github.com/agent-sgs/PillarNet.git>.

## 1 Introduction

With the success in point cloud representation learning using deep neural networks, LiDAR-based 3D object detection has made remarkable progress recently. However, the top-performing point cloud 3D object detectors on the large-scale benchmark datasets, such as nuScenes Dataset [2] and Waymo Open Dataset [39], entail heavy computational load and large memory storage. Hence, it is desirable to develop a top-performing 3D detector with real-time speed for the onboard deployment on autonomous vehicles.

Existing point cloud 3D object detectors mainly use the grid-based representation over point cloud and can be broadly categorized into two groups, *i.e.*, 3D voxel-based and 2D pillar-based methods. Both of these two groups take the classical “encoder-neck-head” detection architecture [10,13,15,28,41,43,47,51,54]. Voxel-based methods [10,13,43,51,54] typically divide the input point cloud into

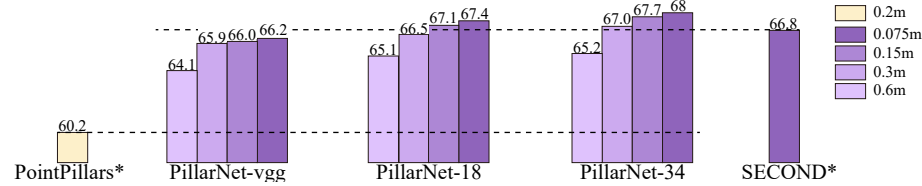


Fig. 1: nuScenes detection score (NDS) comparison between PillarNet variants along with different pillar sizes and two baselines on nuScenes *val* set. The reported results of these two baselines are from latest CenterPoint [49]. All of our PillarNet variants use the same training schedules with CenterPoint-SECOND [49]. \* denotes the reproduction of the two baselines using center-based head.

regular 3D voxel grid. An encoder with sparse 3D convolutions [9] is then used to learn geometric representation across multiple scales. Following the encoder, a neck module with standard 2D CNNs fuses multi-scale features before feeding to the detection head. In contrast, pillar-based methods [15,41,47,28] project 3D point clouds into a 2D pseudo-image on the BEV plane, and then directly build the neck network upon the 2D CNN-based feature pyramid network (FPN) to fuse multi-scale features. For voxel-based methods, the effective voxel-wise feature learning powered by sparse 3D CNN delivers favorable detection performance. However, due to the 3D sparse convolution within the encoder, it is hard to aggregate multi-scale features with different resolutions on the BEV space. For pillar-based methods, a light encoder for pillar feature learning yields unsatisfied performance compared with their voxel-based counterparts. Moreover, the small sized pseudo-image and the large initial pillar further limit the detection performance. It is because a finer pillar leads to larger pseudo-image and more favorable performance but heavier computational load. Interestingly, both voxel- and pillar-based methods perform 3D detection using the aggregated multi-scale features on the BEV space (see Fig. 2).

We observe that previous pillar-based methods do not have powerful pillar feature encoding, which is the main cause of the unsatisfied performance. In addition, progressively downsampling pillar scales can help to decouple the output feature map size and the initial pseudo-image projection scale. As such, we design a real-time and high-performance pillar-based 3D detection method, dubbed PillarNet, that consists of an encoder for hierarchical deep pillar feature extraction, a neck module for multi-scale feature fusion, and the commonly-used center-based detect head. In our PillarNet, the powerful encoder network involves 5 stages. Stage 1 to 4 follow the same setting as the conventional 2D detection networks such as VGG [38] and ResNet [11] but substituted 2D convolutions with its sparse counterparts for resource savings. Stage 5 with standard 2D convolutions possesses a larger receptive field and feeds semantic features to the following neck network. The neck network exchanges sufficient information through stacked convolution layers between the further enriched high-level semantic feature from the encoder stage 5 and the low-level spatial feature from

the encoder stage 4. For tuning the hard-balanced pillar size in previous pillar-based methods, PillarNet offers an effective solution by skillfully detaching the corresponding encoder stages for the chosen pillar scale. For example, to accommodate the input with 8 times pillar size (0.075 \* 8m in nuScenes Dataset), we can simply remove the 1x, 2x, and 4x downsampled encoder stages.

As shown in Fig. 1, our PillarNet with variant configurations, *i.e.*, PillarNet-vgg/18/34, offer the scalability and flexibility for point cloud-based 3D object detection by using merely 2D convolutions. Our PillarNet significantly advances pillar-based 3D detectors and sheds new light on further research on point cloud object detection. Despite its simplicity, the proposed PillarNet achieves the state-of-the-art performance on two large-scale autonomous driving benchmarks [2,39] and runs in real-time (see Sec. 4).

## 2 Related Works

### 2.1 Point Cloud 3D Object Detection

3D object detection with point cloud alone can mainly be summarized into two categories: point-based and grid-based methods.

**Point-based 3D object detectors.** Powered by pioneering PointNet [29,31], point-based methods directly process irregular point clouds and predict 3D bounding boxes. PointRCNN [35] proposes a point-based proposal generation paradigm directly from raw point clouds and then refines each proposal by devising an ROI pooling operation to extract 3D region features. The following work STD [45] transforms interior point features of each proposal into compact voxel representation for better proposal refinement. 3DSSD [22] is a representative one-stage 3D object detector operating on raw points. It also introduces F-FPS as a complement of existing D-FPS during set abstraction layers to benefit regression and classification. These point-based methods naturally preserve accurate point location and enable flexible receptive fields with radius-based local feature aggregation. These methods, however, as summarized in [24], spend 90% of their runtime on organizing irregular point data rather than extracting features, and are not suitable for handling large-scale point clouds.

**Grid-based 3D object detectors.** Most existing methods discrete the sparse and irregular point clouds into regular grids including 3D voxels and 2D pillars, and then capitalize on 2D/3D CNN to perform object detection. The pioneering work VoxelNet [54] divides point cloud into 3D voxels, which are further processed by the voxel feature extractor and 3D CNN encoder network. Due to the sparsity of non-empty voxels in the large outdoor space, SECOND [43] introduces 3D sparse convolution to accelerate VoxelNet [54] and improves the detection accuracy. SA-SSD [10] utilizes two detachable auxiliary networks to guide the 3D CNN encoder to learn fine structure information. Until now, 3D voxel-based methods dominate the majority of 3D detection benchmarks. For a

long time, even with sparse 3D convolution, it was difficult to balance between the high resolution of 3D voxels and the memory and computational complexity.

PointPillars [15] performs 2D voxelization only on the ground plane using a per-pillar feature extractor by PointNet [29], which allows for the use of highly-optimized 2D convolution for the deployment on embedded systems with low latency and computation consumption. MVF [5] leverages multi-view features to augment point-wise information before projecting raw points into 2D pseudo-image. VoxelFPN [41] aggregates multi-scale pseudo-image features from multiple quantized pillar sizes to improve detection performance but the runtime is still dominated by the largest pillar size. Furthermore, HVNet [47] decouples the pseudo-image projection scale and the associated pillar sizes to achieve good accuracy and high inference speed. HVNet first fuses different scales of pillar features at the point-wise level and projects another set of multi-scale 2D pseudo-image feature maps for the encoder network. The recent work HVPR[28] cleverly designs a memory module to update and store point-based features from the 3D voxel-based encoder network during training, and aggregates the point-wise features in memory slots, semantically similar to each voxel-based grid, to obtain a pseudo image representation. The hybrid 3D representation keeps the efficiency of pillar-based detection while implicitly leveraging the voxel-based feature learning regime. Current Pillar-based advancements, however, focus on the sophisticated pillar feature projection and multi-scale aggregation strategies and struggle for narrowing the huge performance gap relative to their voxel-based counterparts. In contrast, we resort to a powerful backbone network to resolve the above problems and boost 3D detection performance.

## 2.2 Multi-sensor based 3D Object Detection

Many approaches attempt to exploit the complementary information from multiple sensors, such as camera image and LiDAR, to detect 3D objects. MV3D [5] designs 3D object anchors and generates proposals from BEV representations and refine them using features from LiDAR in birds-eye-view and images. AVOD [14] instead fuses these features at the stage of generating 3D proposals and provides better detection results. ContFuse [18] fuses image features by learning to project them onto BEV space. MMF [17] learns to fuse the camera and LiDAR features through proxy tasks including depth completion on RGB images and ground estimation from point clouds. 3D-CVF [50] handles the multi-sensor registration case for cross-view spatial feature fusion in the BEV domain. Almost all of these frameworks rely on the BEV representation to perform 3D object detection. Furthermore, their designs are heavyweight due to the complicated fusion strategies. Our method performs 3D detection on BEV space and can be seamlessly integrated into previous multi-sensor 3D object detection framework for advanced performance.

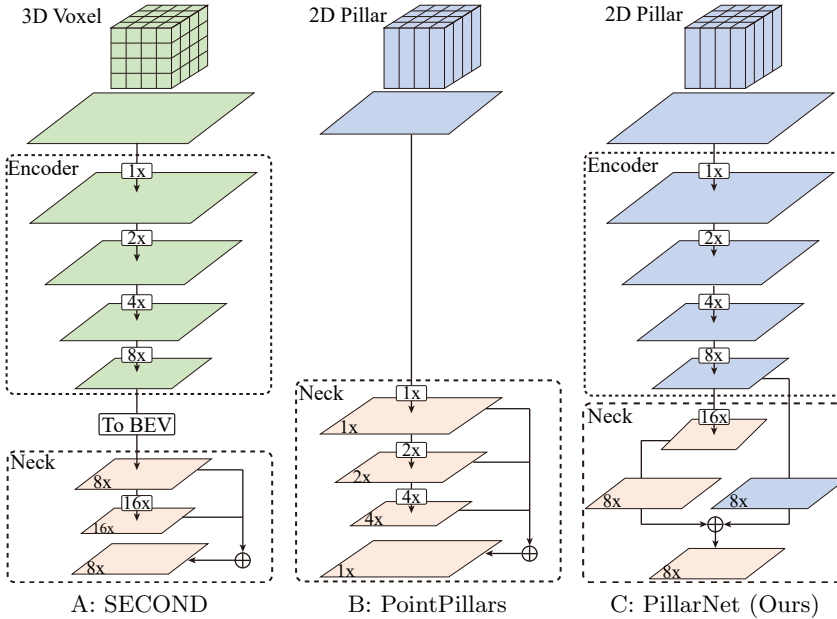


Fig. 2: Comparison of three types of architectures. The encoder uses sparse 3D CNN in SECOND while sparse 2D CNN for PillarNet. The neck in all three methods uses standard 2D CNN. On the nuScenes Dataset, the 3D voxel size in SECOND is (0.075m, 0.075m, 0.2m), and the 2D pillar size in PointPillars and the proposed PillarNet is (0.2m, 0.2m) and (0.075m, 0.075m) respectively.

### 3 PillarNet for 3D Object Detection

#### 3.1 Preliminaries

The grid-based detectors perform 3D detection on BEV space, including 3D voxel-based detectors and 2D pillar-based detectors. Recent voxel-based detectors follow the SECOND [43] architecture with improved sparse 3D CNN for effective voxel feature encoding over pioneering VoxelNet [54]. Pillar-based detectors generally follow the pioneering PointPillars [15] architecture with only 2D CNN for multi-scale feature fusion. We first revisit these two representative point cloud detection architectures, which motivate us to construct the proposed PillarNet method.

**SECOND.** SECOND [43] is a typical voxel-based one-stage object detector, which lays the groundwork for succeeding voxel-based detectors with specialized sparse 3D convolutions [8,9]. It divides the unordered point cloud into regular 3D voxels and performs box prediction on BEV space. The entire 3D detection architecture contains three basic parts: (1) An encoder hierarchically encodes the input non-empty voxel features into 3D feature volumes with the  $1\times$ ,  $2\times$ ,

$4\times$  and  $8\times$  downsampled sizes. (2) A neck module further abstracts the flattened encoder output on the BEV space into multiple scales in a top-down manner. (3) A detect head performs box classification and regression using the fused multi-scale BEV features.

**PointPillars.** PointPillars [15] projects raw point cloud on the X-Y plane via a tiny PointNet [29], yielding a sparse 2D pseudo-image. PointPillars uses a 2D CNN-based top-down network to process the pseudo-image with stride 1x, 2x, and 4x convolution blocks and then concatenates the multi-scale features for the detect head.

**Analysis.** Despite the favorable runtime and memory efficiency, PointPillar [15] still lags far behind SECOND [43] on performance. Under the premise that sparse 3D convolutions possess the superior representation ability for point cloud learning, recent advanced pillar-based methods mainly focus on exploring attentive pillar feature extraction [23,47] from raw points or sophisticated multi-scale strategies [41,47,28]. These methods, on the other hand, suffer from unfavourable latency and still under-performs their 3D voxel-based counterparts by a large margin.

Alternatively, we take a different view by considering grid-based detectors as BEV-based detectors and revisit the entire point cloud learning architecture. We identify that the performance bottleneck of pillar-based methods mainly lies in the sparse encoder network for spatial feature learning and effective neck module for sufficient spatial-semantic features fusion. Specifically, PointPillars directly applies the feature pyramid network to fuse multi-scale features on the projected dense 2D pseudo-image, lacking the sparse encoder network for effective pillar feature encoding as in SECOND. On the other hand, PointPillars couples the size of the final output feature maps with the initial projected pillar scale, increasing the entire calculation and memory cost sharply as the pillar scale gets finer.

To resolve the above issues, we stand by the “encoder-neck-head” detection architecture on BEV space to improve the performance of pillar-based methods. Specifically, we explore the significant difference and respective function for the encoder and neck networks:

- We redesign the encoder in SECOND by substituting sparse 3D convolutions by its sparse 2D convolutions counterpart on loss-less pillar features from raw point clouds. It has been validated in the 3<sup>rd</sup> row of Table 4 that the sparse encoder process enhances 3D detection performance significantly.
- We formulate the neck module as the spatial-semantic feature fusion by inheriting the sparse spatial features from the sparse encoder output and further high-level semantic feature abstraction in low-resolution feature maps, as shown in the 6<sup>th</sup> row of Table 4, which is efficient and effective.

Finally, we build our PillarNet using the relatively heavyweight sparse encoder network for hierarchical pillar feature learning and the lightweight neck module for sufficient spatial-semantic feature fusion.

### 3.2 PillarNet Design for 3D Object Detection

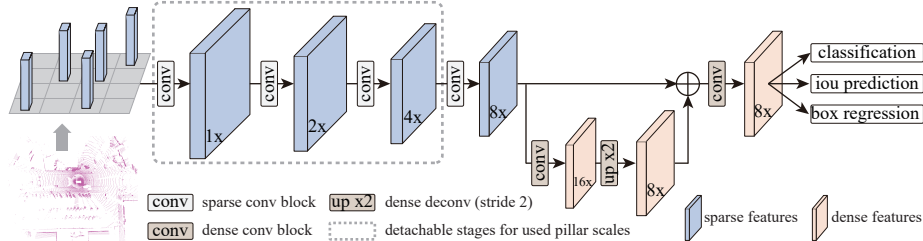


Fig. 3: The overall architecture of our proposed PillarNet. The input point clouds are first quantified into pillars to feed into the 2D sparse convolution-based encoder to learn multi-scale spatial features. Then the densified semantic feature is fused with the spatial feature in the neck module for the final 3D box regression, classification, and IoU prediction.

In this subsection, we present the detailed structure of our PillarNet design. The overall architecture in Fig. 3 consists of three components: the encoder for deep pillar feature extraction, the neck module for spatial-semantic feature aggregation, and the 3D detect head. With the commonly used center-based detect head [49], we present the flexibility and scalability of our PillarNet.

**Encoder design.** The encoder network aims to extract deep sparse pillar features hierarchically from the projected sparse 2D pillar features, where the detachable stages from 1 to 4 progressively down-sample sparse pillar features using sparse 2D CNN. Compared to pioneering PointPillars[15], our designed encoder have two advantages:

- (1) The sparse encoder network can take the progress on image-based 2D object detection, such as VGGNet [37] and ResNet [11]. The simple encoder for pillar feature learning can largely improve 3D detection performance.
- (2) The hierarchically downsampling structure allows PillarNet to skillfully operate the sparse pillar features with different pillar sizes, which alleviates the limitation of coupling pillar size in previous pillar-based methods.

Our constructed PillarNet with variant backbones, PillarNet-vgg/18/34, with the similar complexities of VGGNet/ResNet-18/ResNet-34. The detailed network configurations can be found in the supplementary material.

**Neck design.** The neck module, as in FPN [20], aims to fuse high-level abstract semantic features and low-level fine-grained spatial features for mainstream detect head (*i.e.*, anchor boxes or anchor points). The additional 16X downsampled dense feature maps further abstracts high-level semantic feature using a group of dense 2D CNNs, to enrich receptive field for large objects and populate

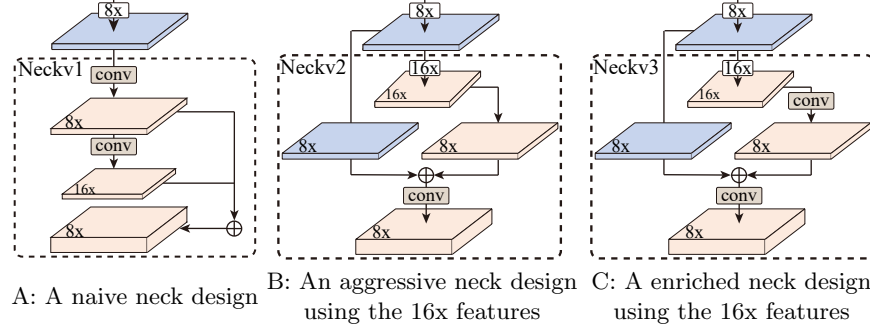


Fig. 4: Detailed structure of different neck designs. The neck A inherits directly from SECOND [43], while two alternative neck designs B and C introduce the spatial features from sparse encoder network and semantic features from the 16X downsampled dense feature maps.

object center-positioned features for center-based detect head. Equipped with sparse spatial features from sparse encoder network, there are two alternative neck designs for the spatial-semantic feature fusion from the starting design in SECOND:

- (1) The naive design neckv1 (Fig. 4(A)) from SECOND [43] applies a top-down network to generate multi-scale features and concatenate multi-scale dense feature maps as the final output.
- (2) The aggressive design neckv2 (Fig. 4(B)) considers sufficient information exchange between high-level semantic feature from additional 16X downsampled dense feature maps and low-level spatial feature from sparse encoder network using a group of convolution layers.
- (3) The design neckv3 (Fig. 4(C)) further enriches the high-level semantic features on 16X downsampled dense feature maps through a group of convolution layers and fuses the spatial-semantic features with the other group of convolution layers for robust feature extraction.

### 3.3 Orientation-Decoupled IoU Regression Loss

In general, the IoU metric highly correlates with the localization quality and classification accuracy of the predicted 3D boxes. Previous methods [19] show that using the 3D IoU quality to reweight the classification and regression scores can achieve better localization accuracy.

For the classification branch, we follow previous methods [13,51] and use the IoU-rectification scheme to incorporate the IoU information into the confidence scores. The IoU-Aware rectification function [13] at the post-processing stage can be formulated as:

$$\hat{S} = S^{1-\beta} * W_{\text{IoU}}^{\beta} \quad (1)$$

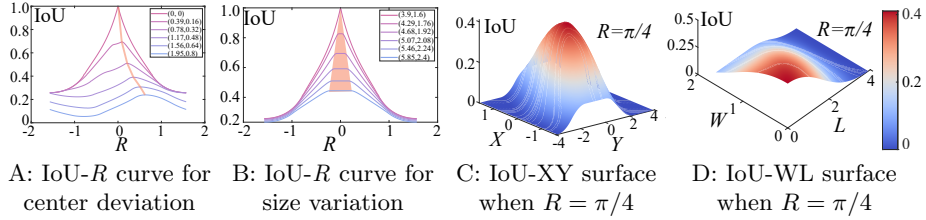


Fig. 5: The IoU metric-based interplay of orientation ( $R$ ) with center or size for a 2D rotated box  $[0, 0, 3.9, 1.6, 0]$ . A and B depict the effect of center variation and size oscillation on orientation regression separately. Red curve in A indicates the local optimum while red region in B for optimization plateau. C and D depict the effect of orientation bias  $R = \pi/4$  on center and size regression separately.

where  $S$  indicates the classification score and  $W_{\text{IoU}}$  is the IoU score.  $\beta$  is a hyper-parameter. For predicting the IoU score, we use L1 loss  $\mathcal{L}_{\text{iou}}$  to supervise the IoU regression, where the target 3D IoU score  $W$  between the predicted 3D box and the ground truth box is encoded by  $2 * (W - 0.5) \in [-1, 1]$ .

For the regression branch, recent methods [19, 52] extend the GIoU [32] loss or DIoU [53] loss from 2D detection to the 3D domain. However, the non-trivial 3D IoU computation slows down the training process. Furthermore, the coupled orientation for the IoU-related regression may negatively affect the training process. Fig. 5 shows such an example. Given a typical 2D bounding box  $[x, y, l, w, \theta] = [0, 0, 3.9, 1.6, 0]$ , there exist cross-effects of orientation with center bias for  $x$  and  $y$  positions or of scale for width and length sizes during the optimization for IoU metric between biased box with ground-truth box as follows:

- The effect of center deviation on orientation regression. The training phase easily settles into a local optimum, if the box center deviates far. See the red curve in Fig. 5(A).
- The effect of size variation on orientation regression. The training phase settles into the notorious optimization plateau, if box sizes change largely. See the red region in Fig. 5(B).
- The effect of orientation bias on center and size regression. The optimization direction remains consistent even if the orientation deviation is significant.

As a result, we present an alternative Orientation-Decoupled IoU-related regression loss by decoupling the orientation  $\theta$  from the mutually-coupled seven parameters  $(x, y, z, w, l, h, \theta)$ . Specifically, we extend the IoU regression loss  $\mathcal{L}_{\text{od-iou}}$  (OD-IoU/OD-GIoU/OD-DIoU) from the IoU loss [32], GIoU loss [32] and DIoU loss [53], respectively.

### 3.4 Overall Loss Function

Following [49], we apply the focal loss [21] for the heatmap classification  $\mathcal{L}_{\text{cls}}$ , and the L1 loss for localization offset  $\mathcal{L}_{\text{off}}$ , the z-axis location  $\mathcal{L}_z$ , 3D object size

$\mathcal{L}_{size}$  and orientation  $\mathcal{L}_{ori}$ . The overall loss  $\mathcal{L}_{total}$  is jointly optimized as follows:

$$\mathcal{L}_{total} = \mathcal{L}_{cls} + \mathcal{L}_{iou} + \lambda(\mathcal{L}_{od-iou} + \mathcal{L}_{off} + \mathcal{L}_z + \mathcal{L}_{size} + \mathcal{L}_{ori}) \quad (2)$$

where the loss weight  $\lambda$  is empirically set parameter as in [49].

## 4 Experiments

**nuScenes Dataset.** nuScenes [2] contains 1000 driving sequences, with 700, 150, 150 sequences for training, validation, and testing, respectively. Each sequence is approximately 20-second long, with a LiDAR frequency of 20 FPS. The dataset provides calibrated vehicle pose information for each LiDAR frame but only provides box annotations every ten frames (0.5s). nuScenes uses a 32 lanes LiDAR, which produces approximately 30k points per frame. The annotations include 10 classes with a long-tail distribution. The official evaluation metrics are mean Average Precision (mAP) and nuScenes detection score (NDS). The mAP defines a match by using a BEV center distance with thresholds of 0.5m, 1m, 2m, 4m. A new metric, NDS, on the basis of 2m center distance matching threshold, calculates the weighted sum of a set of true positive metrics that measure translation, scale, orientation, velocity and attribute errors. We follow the convention to accumulate 10 LiDAR sweeps to densify the point clouds and report results by using the official evaluation protocol.

**Waymo Open Dataset.** Waymo Open Dataset [39] is currently the largest dataset with LiDAR point clouds for autonomous driving. There are total 798 training sequences with around 160k LiDAR samples, and 202 validation sequences with 40k LiDAR samples. It annotated the objects in the full 360° field. The evaluation metrics are calculated by the official evaluation tools, where the mean average precision (mAP) and the mean average precision weighted by heading (mAPH) are used for evaluation. The 3D IoU threshold is set as 0.7 for vehicle detection and 0.5 for pedestrian/cyclist detection. We present the comparison in terms of two ways. The first way is based on objects' different distances to the sensor: 0 – 30m, 30m – 50m and > 50m. The second way is to split the data into two difficulty levels, where the LEVEL.1 denotes the ground-truth objects with at least 5 inside points while the LEVEL.2 denotes the ground-truth objects with at least 1 inside point.

**Training and Inference details.** We use the same training schedules as prior CenterPoint [49], where Adam optimizer is used with one-cycle learning rate policy, weight decay 0.01, and momentum 0.85 to 0.95 on 4 Tesla V100 GPUs. We compare our method with the baselines (*i.e.*, *CenterPoint-SECOND* and *CenterPoint-PointPillars*) on another PC equipped with an i9 CPU and RTX 3090 GPU instead of the above cluster server. During the pillar feature projection from the raw point clouds, we augment the point-wise features of all inside points per pillar with the Euclidean distance to the center of that pillar. Then one-layer

MLP-based PointNet transforms the point-wise features and pools them using *atomic max* operation based on GPU.

We adopt the widely used data augmentation strategies during training, including the random scene flipping along both X and Y axes, random rotation around Z axis with a random factor from  $[-\pi/4, \pi/4]$ , random scene scaling with a random factor sampled from  $[0.95, 1.05]$ , and random translation with a random factor from  $[-0.5m, 0.5m]$ . We use the context-aware ground-truth sampling augmentation technique, where we collect all the inside points around the enlarged 3D ground-truth boxes with an extra scale of 1.2 to pre-built the GT database. During training, we randomly select some ground-truth boxes from the GT database and place them into the current training scene.

For nuScenes Dataset, we set the detection range to  $[-54m, 54m]$  for the X and Y axis, and  $[-5m, 3m]$  for the Z axis. The voxel size for the baseline SECOND [43] is kept as  $(0.075m, 0.075m, 0.2m)$ , and the pillar size for the baseline PointPillars [15] is hold as  $(0.2m, 0.2m)$  on the ground plane. For our PillarNet, we use  $(0.075m, 0.075m)$  as the basic pillar size for experiments. We train the PillarNet from scratch with batch size 16, max learning rate 1e-3 for 20 epochs. For the post-processing process during inference, following [49], we use class-agnostic NMS with the score threshold set to 0.2 and rectification factor  $\beta$  to 0.5 for all 10 classes. We do not use any model ensembling except double-flip test-time augmentation as CenterPoint [49] on nuScenes Dataset.

For Waymo Open Dataset, we set the detection range to  $[-75.2m, 75.2m]$  for both the X and Y axes, and  $[-2m, 4m]$  for the Z axis. The voxel size for the baseline SECOND [43] is kept as  $(0.1m, 0.1m, 0.15m)$ , and the pillar size for the baseline PointPillars [15] is hold as  $(0.32m, 0.32m)$  on the ground plane. For our PillarNet, we use  $(0.1m, 0.1m)$  as the basic setting for experiments. We train the PillarNet from scratch with batch size 16, max learning rate 3e-3 for 36 epochs. For the post-processing process during inference, following [13], we use class-specific NMS with the IoU threshold set to 0.8, 0.55, 0.55 and rectification factor  $\beta$  to 0.68, 0.71, 0.65 for Vehicle, Pedestrian and Cyclist respectively.

#### 4.1 Overall Results

**Evaluation on nuScenes *test* set.** We also compare our PillarNet variants with previous LiDAR-only non-ensemble methods on the nuScenes *test* set. As shown in Table 1, all our PillarNet-vgg/18/34 go beyond the stage-of-the-art methods by a large margin while running at a real-time speed of 14, 13 and 12 FPS, respectively. In addition, the promising results of PillarNet variants validate the good scalability of our PillarNet, where the performance behaves more favorably as the computational complexity rises. Typically, PillarNet-18 surprisingly surpasses the most advanced AFDetV2 by +2.3% NDS or +2.6% mAP. To the best of our knowledge, PillarNet-vgg/18/34 surpasses all the published LiDAR-only non-ensemble methods on the nuScenes Detection leaderboard on Mar 7, 2022. From this point on, PillarNet achieves new state-of-the-art performance using only 2D convolutions.

Methods	Stages	NDS mAP	Car	Truck	Bus	Trailer	Cons.Veh.	Ped.	Motor.	Bicycle	Tr.Cone	Barrier
WYSIWYG [12]	One	41.9 35.0	79.1	30.4	46.6	40.1	7.1	65.0	18.2	0.1	28.8	34.7
PointPillars [15]	One	45.3 30.5	68.4	23.0	28.2	23.4	4.1	59.7	27.4	1.1	30.8	38.9
3DVID [48]	One	53.1 45.4	79.7	33.6	47.1	43.1	18.1	76.5	40.7	7.9	58.8	48.8
3DSSD [44]	One	56.4 42.6	81.2	47.2	61.4	30.5	12.6	70.2	36.0	8.6	31.1	47.9
Cylinder3D [56]	One	61.6 50.6	-	-	-	-	-	-	-	-	-	-
CGBS [55]	One	63.3 52.8	81.1	48.5	54.9	42.9	10.5	80.1	51.5	22.3	70.9	65.7
CVCNet [3]	One	64.2 55.8	82.6	49.5	59.4	51.1	16.2	83.0	61.8	38.8	69.7	69.7
CenterPoint [49]	Two	65.5 58.0	84.6	51.0	60.2	53.2	17.5	83.4	53.7	28.7	76.7	70.9
HotSpotNet [4]	One	66.0 59.3	83.1	50.9	56.4	53.3	23.0	81.3	63.5	36.6	73.0	71.6
AFDetV2 [13]	One	68.5 62.4	86.3	54.2	62.5	58.9	26.7	85.8	63.8	34.3	80.1	71.0
PillarNet-vgg	One	69.6 63.3	86.9	56.0	62.2	62.0	28.6	86.3	62.6	33.5	79.6	75.6
PillarNet-18	One	70.8 65.0	87.4	56.7	60.9	61.8	<b>30.4</b>	87.2	67.4	40.3	82.1	76.0
PillarNet-34	One	<b>71.4 66.0</b>	<b>87.6</b>	<b>57.5</b>	<b>63.6</b>	<b>63.1</b>	27.9	<b>87.3</b>	<b>70.1</b>	<b>42.3</b>	<b>83.3</b>	<b>77.2</b>

Table 1: The LiDAR-only non-ensemble 3D detection performance comparison on the nuScenes *test* set. The table is mainly sorted by nuScenes detection score (NDS) which is the official ranking metric.

**Evaluation on Waymo Open Dataset *test* set.** We also compare our PillarNet variants with all the published methods on the Waymo Open Dataset *test* set in Table 2. Table 2 contains two groups, where the upper group is single-frame LiDAR-only non-ensemble methods and the bottom group is multi-frame LiDAR-only non-ensemble methods.

Our PillarNet-18/34 outperforms all the previous single-frame and multi-frame LiDAR-only models for the vehicle and pedestrian categories while running at a speed of 20/17 FPS separately. Our lightweight PillarNet-vgg still achieves the comparable performance for the vehicle while running at a faster speed of 23 FPS. Using merely 2D convolutions, our real-time PillarNet variants are suitable for onboard deployment.

**Evaluation on Waymo Open Dataset *val* set.** We compare our PillarNet variants with all published single-frame LiDAR-only non-ensemble methods on WOD *val* set in Table 3. We also present the performance of PillarNet variants based on two-frame-merged LiDAR points for reference. Typically, PillarNet-18 achieves the state-of-the-art performance on the vehicle category, making it a viable replacement for previous state-of-the-art 3D voxel-based methods. Our PillarNet-34 outperforms previous state-of-the-art works with remarkable performance gains (+1.24 for the vehicle in terms of mAPH of LEVEL\_2 difficulty). Excluding the latest voxel-based detector AFDetV2 using the self-calibrated neck network and intrinsic channel-wise and spatial-wise attention, PillarNet-34 outperforms the previous one-stage and two-stage 3D detectors in all three categories while operating at super real-time speed.

## 4.2 Ablation Studies

In this section, we investigate the individual components of the proposed PillarNet with extensive ablation experiments on the *val* set of nuScenes Dataset.

Methods	Stages	Sensors	Frames	Vehicle (L1) mAP mAPH	Vehicle (L2) mAP mAPH	Ped. (L1) mAP mAPH	Ped. (L2) mAP mAPH	Cyc. (L1) mAP mAPH	Cyc. (L2) mAP mAPH
StarNet [27]	Two	-	1	61.50 61.00	54.90 54.50	67.80 59.90	61.10 54.00	- -	- -
† PointPillars [15]	One	LT	1	68.60 68.10	60.50 60.10	68.00 55.50	61.40 50.10	- -	- -
RCD [1]	Two	-	1	71.97 71.59	65.06 64.70	- -	- -	- -	- -
Light-FMFNet [26]	One	L	1	77.85 77.30	70.16 69.65	69.52 59.78	63.62 54.61	66.34 64.69	63.87 62.28
HIKVISION.LiDAR [42]	Two	L	1	78.63 78.14	71.06 70.60	76.00 69.90	69.82 64.11	70.94 69.70	68.35 67.15
CenterPoint [49]	Two	LT	1	80.20 79.70	72.20 71.80	78.30 72.10	72.20 66.40	- -	- -
AFDetV2 [13]	One	LT	1	80.49 80.43	72.98 72.55	79.76 74.35	73.71 68.61	<b>72.43</b> <b>71.23</b>	<b>69.84</b> <b>68.67</b>
PillarNet-vgg	One	LT	1	<b>81.16</b> <b>80.68</b>	<b>73.64</b> <b>73.20</b>	78.30 70.28	72.23 64.68	67.26 66.07	64.79 63.65
PillarNet-18	One	LT	1	<b>81.85</b> <b>81.40</b>	<b>74.46</b> <b>74.03</b>	<b>79.97</b> <b>72.63</b>	<b>73.95</b> <b>67.09</b>	67.98 66.80	65.50 64.36
PillarNet-34	One	LT	1	<b>82.47</b> <b>82.03</b>	<b>75.07</b> <b>74.65</b>	<b>80.82</b> <b>74.13</b>	<b>74.83</b> <b>68.54</b>	69.08 67.91	66.60 65.47
3D-MAN [46]	Multi	L	15	78.71 78.28	70.37 69.98	69.97 65.98	63.98 60.26	- -	- -
RSN [40]	Two	LT	3	80.70 80.30	71.90 71.60	78.90 75.60	70.70 67.80	- -	- -
CenterPoint [49]	Two	L	2	81.05 80.59	73.42 72.99	80.47 77.28	74.56 71.52	74.60 73.68	72.17 71.28
Pyramid R-CNN [25]	Two	L	2	81.77 81.32	74.87 74.43	- -	- -	- -	- -
AFDetV2 [13]	One	LT	2	81.65 81.22	74.30 73.89	81.26 78.05	75.47 72.41	<b>76.41</b> <b>75.37</b>	<b>74.05</b> <b>73.04</b>
PillarNet-vgg	One	LT	2	<b>82.18</b> <b>81.73</b>	<b>74.93</b> <b>74.49</b>	80.41 76.86	74.52 71.14	68.75 67.89	66.52 65.68
PillarNet-18	One	LT	2	<b>82.68</b> <b>82.25</b>	<b>75.53</b> <b>75.12</b>	<b>81.71</b> <b>78.29</b>	<b>75.91</b> <b>72.66</b>	70.19 69.30	68.01 67.15
PillarNet-34	One	LT	2	<b>83.23</b> <b>82.80</b>	<b>76.09</b> <b>75.69</b>	<b>82.38</b> <b>79.02</b>	<b>76.66</b> <b>73.46</b>	71.44 70.51	69.20 68.29

Table 2: Single- (upper group) and multi-frame (lower group) LiDAR-only non-ensemble performance comparison on the Waymo Open Dataset *test* set. "L" and "LT" mean "all LiDARs" and "top-LiDAR only", respectively. † denotes the reported results from RSN [40].

**Analysis of PillarNet improvements.** The key contribution of our work can be divided into two parts: the designed PillarNet architecture (*i.e.*, encoder and neck module) and the IoU-related modules (*i.e.*, Orientation-Decoupled IoU (OD-IoU) regression loss and IoU-Aware rectification). For the first part, we will analyze how our designed encoder and neck networks improve the 3D detection performance. To fairly compare with two known baselines (PointPillars [15] and SECOND [43]), all of them use the identical center-based detect head and PillarNet adopts the same hyper-parameters settings as SECOND. It's worth noting that the well-trained baseline models come from the latest code-base<sup>1</sup>.

**Encoder network.** Compared with pioneering PointPillars [15] in 1<sup>st</sup> row of Table 4, our newly introduced encoder network from stage 1 to 4 could significantly improve the detection performance by about +7.61% mAP and +5.94% NDS. Using the heavy encoder structure with additional stage 5 in 3<sup>rd</sup> to 6<sup>th</sup> rows could boost the 3D detection performance by a large margin. In addition, using the further enriched semantic features from encoder stage 5 in 4<sup>th</sup> to 5<sup>th</sup> rows perform better than aggressive fusion strategy in 6<sup>th</sup> row.

**Neck network.** We propose two novel neck structures (*i.e.*, neckv2 and neckv3 in Fig. 4) for spatial-semantic feature fusion, which involves the low-level spatial features from encoder stage 4 and high-level semantic features from additional encoder stage 5. Compared with the naive neckv1 in Fig. 4, as shown in Table 4, our fusion design from 4<sup>th</sup> to 6<sup>th</sup> rows by using a group of convolution layers could improve detection performance by a large margin. Additionally, the further semantic feature enrichment in 4<sup>th</sup> and 5<sup>th</sup> rows could obtain better performance than the simple concatenation in 6<sup>th</sup> row. The performance difference between neckv2 and neckv2-*D* shows that the dense convolutions enable stronger semantic

<sup>1</sup> <https://github.com/tianweiy/CenterPoint>

Methods	Stages	Vehicle (L1)		Vehicle (L2)		Ped. (L1)		Ped. (L2)		Cyc. (L1)		Cyc. (L2)	
		mAP	mAPH										
StarNet [27]	Two	53.70	-	-	-	66.80	-	-	-	-	-	-	-
MVF [5]	One	62.93	-	-	-	65.33	-	-	-	-	-	-	-
CVCNet [3]	One	65.20	-	-	-	-	-	-	-	-	-	-	-
3D-MAN [46]	Multi	69.03	68.52	60.16	59.71	71.71	67.74	62.58	59.04	-	-	-	-
RCD [1]	Two	69.59	69.16	-	-	-	-	-	-	-	-	-	-
Pillar-based [43]	One	69.80	-	-	-	72.51	-	-	-	-	-	-	-
†SECOND [43]	One	72.27	71.69	63.85	63.33	68.70	58.18	60.72	51.31	60.62	59.28	58.34	57.05
†PointPillar [15]	One	56.62	-	-	-	59.25	-	-	-	-	-	-	-
LiDAR R-CNN [16]	Two	73.50	73.00	64.70	64.20	71.20	58.70	63.10	51.70	68.60	66.90	66.10	64.40
RangeDet [7]	One	72.85	-	-	-	75.94	-	-	-	65.80	-	-	-
MVF++ [30]	One	74.64	-	-	-	78.01	-	-	-	-	-	-	-
RSN [40]	Two	75.10	74.60	66.00	65.50	77.80	72.70	68.30	63.70	-	-	-	-
Voxel R-CNN [6]	Two	75.59	-	66.59	-	-	-	-	-	-	-	-	-
CenterPoint [49]	Two	76.70	76.20	68.80	68.30	79.00	72.90	71.00	65.30	-	-	-	-
Part-A <sup>2</sup> [36]	Two	77.05	76.51	68.47	67.97	75.24	66.87	66.18	58.62	68.60	67.36	66.13	64.93
PV-RCNN [33]	Two	77.51	76.89	68.98	68.41	75.01	65.65	66.04	57.61	67.81	66.35	65.39	63.98
AFDetV2 [13]	One	77.64	77.14	69.68	69.22	80.19	<b>74.62</b>	72.16	<b>66.95</b>	<b>73.72</b>	<b>72.74</b>	<b>71.06</b>	<b>70.12</b>
Two-frame 3D detection results of PillarNet variants for reference.													
PillarNet-vgg	One	77.41	76.86	69.46	68.96	78.30	70.32	70.00	62.62	69.48	68.35	66.87	65.78
PillarNet-18	One	78.24	77.73	70.40	69.92	79.80	72.59	71.57	64.90	70.40	69.29	67.75	66.68
PillarNet-34	One	<b>79.09</b>	<b>78.59</b>	<b>70.92</b>	<b>70.46</b>	<b>80.59</b>	74.01	<b>72.28</b>	66.17	72.29	71.21	69.72	68.67

Table 3: The single-frame LiDAR-only non-ensemble 3D AP/APH performance comparison on the Waymo Open Dataset *val* set. †: reported by [16].

abstraction at the object center than the sparse convolutions, according to the fact that LiDAR points are sparsely scattered on the surface of the objects.

*OD-IoU regression loss.* Our proposed orientation-decoupled regression loss includes three variants, *i.e.*, OD-IoU, OD-GIoU and OD-DIoU. All three types of losses play a role in the critical positioning accuracy, while the OD-DIoU loss brings a maximum boost with +0.24% mAP or +0.24% NDS.

*IoU-Aware rectification.* The IoU-Aware rectification module alleviates the misalignment between localization confidence and classification score. Adding IoU-Aware rectification benefits the IoU-based mAP with +0.34% increase.

**Analysis of model variants.** We investigate the effectiveness of PillarNet variants which have different FLOPs complexity by detaching OD-IoU regression loss and IoU rectification modules for a clean comparison. The PillarNet-vgg/18/34 only differs in the number of convolution blocks in each stage while keeping the other structures the same. The results are shown in Table 5: our designed PillarNet could benefit from increasing model capacity with slightly more FLOPs and inference time. The scalability of PillarNet provides a very useful guide for engineering practices according to practical needs.

**Analysis of pillar sizes.** We investigate the impact of pillar size on 3D detection performance without using OD-IoU regression loss and IoU rectification modules for a clean comparison. Specifically, we castrate the corresponding encoder stages to accommodate the PillarNet for different pillar scales, where larger

Methods	FPS	mAP	NDS	mATE	mASE	mAOE	mAVE	mAAE
†PointPillars [15]	31	50.26	60.22	31.32	25.94	39.50	32.54	19.79
†SECOND [43]	8	59.56	66.76	29.22	25.51	30.24	25.91	19.34
PointPillars (0.075m) <sup>1</sup>	9	50.26	60.22	31.32	25.94	39.50	32.54	19.79
PillarNet-18(neckv1)	17	57.87	66.16	29.88	26.05	27.86	25.78	18.14
PillarNet-18(neckv2)	16	59.40	66.96	29.07	25.86	29.61	24.69	18.17
PillarNet-18(neckv2-D)	16	59.48	67.15	29.03	25.83	27.54	24.54	18.90
PillarNet-18(neckv3)	16	58.53	66.41	29.82	26.05	29.56	24.53	18.65
PillarNet-18(OD-IoU)	16	59.51	67.09	28.51	25.57	29.31	24.63	18.64
PillarNet-18(OD-GIoU)	16	59.69	67.35	28.50	25.78	27.57	24.74	18.37
PillarNet-18(OD-DIoU)	16	59.72	67.39	28.40	25.81	27.38	24.67	18.41
PillarNet-18(IoU)	16	59.82	67.16	28.92	25.53	28.37	25.63	19.07
PillarNet-18	16	59.90	67.39	27.72	25.20	28.93	24.67	19.11

Table 4: The analysis of each component of PillarNet with the same training schedules as SECOND and also comparison with the two baselines (*i.e.*, PointPillars and SECOND) on nuScenes *val* dataset. †: reported by used codebase.

Models	FPS	mAP	NDS
PillarNet-vgg	16	57.67	65.71
PillarNet-18	16	59.41	67.09
PillarNet-34	14	59.98	67.50

Table 5: The effect of different PillarNet variants by detaching two IoU-related modules.

Pillar size	FPS	encoder stages	mAP	NDS
0.075m	16	(1x 2x 4x 8x 16x)	59.48	67.15
0.075*2m	16	(2x 4x 8x 16x)	58.70	66.56
0.075*4m	16	(4x 8x 16x)	57.87	66.05
0.075*8m	14	(8x 16x)	55.37	64.20

Table 6: The effect of different pillar sizes and its associated stages in PillarNet-18 encoder.

pillar sizes correspond to a more reduced encoder structure. From Table 6 and Fig 1, we can see that PillarNet can benefit from finer pillar scale and deeper pillar feature encoding. On the other hand, PointPillars [15] with finer 0.075m in 3<sup>rd</sup> row of Table 4 performs slightly worse than PointPillars of 0.2m, because small pillar size is less robust to object scale variance give its architecture. This implies the importance of hierarchical pillar feature encoding of PillarNet for better performance. The slow inference speed for PillarNet with coarser pillar size and reduced encoder stages may be due to the fact that cuda *atomic max* operation struggles to handle more inside points per pillar based on global memory. The much higher performance in 3<sup>rd</sup> and 4<sup>th</sup> rows of Table 6 over PointPillars with 0.2m demonstrates the effectiveness and efficiency of our PillarNet design. The flexibility of PillarNet provides guidance on the trade-off between performance and model complexity according to practical demands.

**Runtime analysis.** We also evaluate the runtime of our PillarNet as well as baseline single-stage counterparts (PointPillars [15] and SECOND [43]) during inference, by using the reported models from codebase<sup>1</sup> on the same platform for a fair comparison. As shown in Table 7, PillarNet-18 runs much faster than CenterPoint-VoxelNet on the nuScenes Dataset. On the Waymo Dataset with more environmental coverage, PillarNet-18 runs faster than CenterPoint-

PointPillars as well. This demonstrates that PillarNet scales well and maintains a good balance between accuracy and speed.

Method	Waymo (FPS)	nuScenes (FPS)
CenterPoint-PointPillars <sup>1</sup>	19	31
CenterPoint-VoxelNet <sup>1</sup>	9	8
PillarNet-18 (Ours)	21	16

Table 7: Runtime comparison of different methods during inference.

## 5 Conclusions

In this work, we propose a real-time and high-performance one-stage 3D object detector. From the perspective of “encoder-neck-head” architecture design, PillarNet achieves the scalability and flexibility for the hard-balanced pillar size and model complexities. Furthermore, we propose the Orientation-Decoupled regression loss along with the IoU-Aware rectification module for better 3D bounding box optimization during training. Extensive experiments on two large-scale autonomous driving benchmarks demonstrate that our PillarNet achieves the new state-of-the-art performance with merely 2D convolutions while running at real-time speed. We expect that our findings will stimulate further research into pillar-based point cloud representation learning.

## References

1. Bewley, A., Sun, P., Mensink, T., Anguelov, D., Sminchisescu, C.: Range conditioned dilated convolutions for scale invariant 3d object detection. In: Conference on Robot Learning (CoRL) (2020)
2. Caesar, H., Bankiti, V., Lang, A.H., Vora, S., Liang, V.E., Xu, Q., Krishnan, A., Pan, Y., Baldan, G., Beijbom, O.: nuscenes: A multimodal dataset for autonomous driving. In: Proceedings of the IEEE/CVF conference on computer vision and pattern recognition. pp. 11621–11631 (2020)
3. Chen, Q., Sun, L., Cheung, E., Yuille, A.L.: Every view counts: Cross-view consistency in 3d object detection with hybrid-cylindrical-spherical voxelization. Advances in Neural Information Processing Systems **33**, 21224–21235 (2020)
4. Chen, Q., Sun, L., Wang, Z., Jia, K., Yuille, A.: Object as hotspots: An anchor-free 3d object detection approach via firing of hotspots. In: European conference on computer vision. pp. 68–84. Springer (2020)
5. Chen, X., Ma, H., Wan, J., Li, B., Xia, T.: Multi-view 3d object detection network for autonomous driving. In: Proceedings of the IEEE conference on Computer Vision and Pattern Recognition. pp. 1907–1915 (2017)
6. Deng, J., Shi, S., Li, P., Zhou, W., Zhang, Y., Li, H.: Voxel r-cnn: Towards high performance voxel-based 3d object detection. In: Proceedings of the AAAI Conference on Artificial Intelligence (2021)
7. Fan, L., Xiong, X., Wang, F., Wang, N., Zhang, Z.: Rangedet: In defense of range view for lidar-based 3d object detection. In: Proceedings of the IEEE/CVF International Conference on Computer Vision. pp. 2918–2927 (2021)
8. Graham, B., Engelcke, M., Van Der Maaten, L.: 3d semantic segmentation with submanifold sparse convolutional networks. In: Proceedings of the IEEE conference on computer vision and pattern recognition. pp. 9224–9232 (2018)
9. Graham, B., van der Maaten, L.: Submanifold sparse convolutional networks. arXiv preprint arXiv:1706.01307 (2017)
10. He, C., Zeng, H., Huang, J., Hua, X.S., Zhang, L.: Structure aware single-stage 3d object detection from point cloud. In: Proceedings of the IEEE/CVF Conference on Computer Vision and Pattern Recognition. pp. 11873–11882 (2020)
11. He, K., Zhang, X., Ren, S., Sun, J.: Deep residual learning for image recognition. In: Proceedings of the IEEE conference on computer vision and pattern recognition. pp. 770–778 (2016)
12. Hu, P., Ziglar, J., Held, D., Ramanan, D.: What you see is what you get: Exploiting visibility for 3d object detection. In: Proceedings of the IEEE/CVF Conference on Computer Vision and Pattern Recognition. pp. 11001–11009 (2020)
13. Hu, Y., Ding, Z., Ge, R., Shao, W., Huang, L., Li, K., Liu, Q.: Afdetv2: Rethinking the necessity of the second stage for object detection from point clouds (2021)
14. Ku, J., Mozifian, M., Lee, J., Harakeh, A., Waslander, S.L.: Joint 3d proposal generation and object detection from view aggregation. In: 2018 IEEE/RSJ International Conference on Intelligent Robots and Systems (IROS). pp. 1–8. IEEE (2018)
15. Lang, A.H., Vora, S., Caesar, H., Zhou, L., Yang, J., Beijbom, O.: Pointpillars: Fast encoders for object detection from point clouds. In: Proceedings of the IEEE/CVF Conference on Computer Vision and Pattern Recognition. pp. 12697–12705 (2019)
16. Li, Z., Wang, F., Wang, N.: Lidar r-cnn: An efficient and universal 3d object detector. In: Proceedings of the IEEE/CVF Conference on Computer Vision and Pattern Recognition. pp. 7546–7555 (2021)

17. Liang, M., Yang, B., Chen, Y., Hu, R., Urtasun, R.: Multi-task multi-sensor fusion for 3d object detection. In: Proceedings of the IEEE/CVF Conference on Computer Vision and Pattern Recognition. pp. 7345–7353 (2019)
18. Liang, M., Yang, B., Wang, S., Urtasun, R.: Deep continuous fusion for multi-sensor 3d object detection. In: Proceedings of the European conference on computer vision (ECCV). pp. 641–656 (2018)
19. Liang, Z., Zhang, Z., Zhang, M., Zhao, X., Pu, S.: Rangeioudet: Range image based real-time 3d object detector optimized by intersection over union. In: Proceedings of the IEEE/CVF Conference on Computer Vision and Pattern Recognition. pp. 7140–7149 (2021)
20. Lin, T.Y., Dollár, P., Girshick, R., He, K., Hariharan, B., Belongie, S.: Feature pyramid networks for object detection. In: Proceedings of the IEEE conference on computer vision and pattern recognition. pp. 2117–2125 (2017)
21. Lin, T.Y., Goyal, P., Girshick, R., He, K., Dollár, P.: Focal loss for dense object detection. In: Proceedings of the IEEE international conference on computer vision. pp. 2980–2988 (2017)
22. Liu, W., Anguelov, D., Erhan, D., Szegedy, C., Reed, S., Fu, C.Y., Berg, A.C.: Ssd: Single shot multibox detector. In: European conference on computer vision. pp. 21–37. Springer (2016)
23. Liu, Z., Zhao, X., Huang, T., Hu, R., Zhou, Y., Bai, X.: Tanet: Robust 3d object detection from point clouds with triple attention. In: Proceedings of the AAAI Conference on Artificial Intelligence. vol. 34, pp. 11677–11684 (2020)
24. Liu, Z., Tang, H., Lin, Y., Han, S.: Point-voxel cnn for efficient 3d deep learning. Advances in Neural Information Processing Systems **32** (2019)
25. Mao, J., Niu, M., Bai, H., Liang, X., Xu, H., Xu, C.: Pyramid r-cnn: Towards better performance and adaptability for 3d object detection. In: Proceedings of the IEEE/CVF International Conference on Computer Vision. pp. 2723–2732 (2021)
26. Murhij, Y., Yudin, D.: Real-time 3d object detection using feature map flow. arXiv preprint arXiv:2106.14101 (2021)
27. Ngiam, J., Caine, B., Han, W., Yang, B., Chai, Y., Sun, P., Zhou, Y., Yi, X., Alsharif, O., Nguyen, P., et al.: Starnet: Targeted computation for object detection in point clouds. arXiv preprint arXiv:1908.11069 (2019)
28. Noh, J., Lee, S., Ham, B.: Hvpr: Hybrid voxel-point representation for single-stage 3d object detection. In: Proceedings of the IEEE/CVF Conference on Computer Vision and Pattern Recognition. pp. 14605–14614 (2021)
29. Qi, C.R., Su, H., Mo, K., Guibas, L.J.: Pointnet: Deep learning on point sets for 3d classification and segmentation. In: Proceedings of the IEEE conference on computer vision and pattern recognition. pp. 652–660 (2017)
30. Qi, C.R., Zhou, Y., Najibi, M., Sun, P., Vo, K., Deng, B., Anguelov, D.: Offboard 3d object detection from point cloud sequences. In: Proceedings of the IEEE/CVF Conference on Computer Vision and Pattern Recognition. pp. 6134–6144 (2021)
31. Qi, C.R., Yi, L., Su, H., Guibas, L.J.: Pointnet++: Deep hierarchical feature learning on point sets in a metric space. Advances in neural information processing systems **30** (2017)
32. Rezatofighi, H., Tsoi, N., Gwak, J., Sadeghian, A., Reid, I., Savarese, S.: Generalized intersection over union: A metric and a loss for bounding box regression. In: Proceedings of the IEEE/CVF conference on computer vision and pattern recognition. pp. 658–666 (2019)
33. Shi, S., Guo, C., Jiang, L., Wang, Z., Shi, J., Wang, X., Li, H.: Pv-rcnn: Point-voxel feature set abstraction for 3d object detection. In: Proceedings of the IEEE/CVF Conference on Computer Vision and Pattern Recognition. pp. 10529–10538 (2020)

34. Shi, S., Jiang, L., Deng, J., Wang, Z., Guo, C., Shi, J., Wang, X., Li, H.: Pv-rcnn++: Point-voxel feature set abstraction with local vector representation for 3d object detection. arXiv preprint arXiv:2102.00463 (2021)
35. Shi, S., Wang, X., Li, H.: Pointrcnn: 3d object proposal generation and detection from point cloud. In: Proceedings of the IEEE/CVF conference on computer vision and pattern recognition. pp. 770–779 (2019)
36. Shi, S., Wang, Z., Shi, J., Wang, X., Li, H.: From points to parts: 3d object detection from point cloud with part-aware and part-aggregation network. IEEE transactions on pattern analysis and machine intelligence **43**(8), 2647–2664 (2020)
37. Simonyan, K., Zisserman, A.: Two-stream convolutional networks for action recognition in videos. Advances in neural information processing systems **27** (2014)
38. Simonyan, K., Zisserman, A.: Very deep convolutional networks for large-scale image recognition. arXiv preprint arXiv:1409.1556 (2014)
39. Sun, P., Kretzschmar, H., Dotiwalla, X., Chouard, A., Patnaik, V., Tsui, P., Guo, J., Zhou, Y., Chai, Y., Caine, B., et al.: Scalability in perception for autonomous driving: Waymo open dataset. In: Proceedings of the IEEE/CVF conference on computer vision and pattern recognition. pp. 2446–2454 (2020)
40. Sun, P., Wang, W., Chai, Y., Elsayed, G., Bewley, A., Zhang, X., Sminchisescu, C., Anguelov, D.: Rsn: Range sparse net for efficient, accurate lidar 3d object detection. In: Proceedings of the IEEE/CVF Conference on Computer Vision and Pattern Recognition. pp. 5725–5734 (2021)
41. Wang, B., An, J., Cao, J.: Voxel-fpn: multi-scale voxel feature aggregation in 3d object detection from point clouds. arXiv preprint arXiv:1907.05286 (2019)
42. Xu, J., Tang, X., Dou, J., Shu, X., Zhu, Y.: Centeratt: Fast 2-stage center attention network. arXiv preprint arXiv:2106.10493 (2021)
43. Yan, Y., Mao, Y., Li, B.: Second: Sparsely embedded convolutional detection. Sensors **18**(10), 3337 (2018)
44. Yang, Z., Sun, Y., Liu, S., Jia, J.: 3dssd: Point-based 3d single stage object detector. In: Proceedings of the IEEE/CVF conference on computer vision and pattern recognition. pp. 11040–11048 (2020)
45. Yang, Z., Sun, Y., Liu, S., Shen, X., Jia, J.: Std: Sparse-to-dense 3d object detector for point cloud. In: Proceedings of the IEEE/CVF International Conference on Computer Vision. pp. 1951–1960 (2019)
46. Yang, Z., Zhou, Y., Chen, Z., Ngiam, J.: 3d-man: 3d multi-frame attention network for object detection. In: Proceedings of the IEEE/CVF Conference on Computer Vision and Pattern Recognition. pp. 1863–1872 (2021)
47. Ye, M., Xu, S., Cao, T.: Hvnet: Hybrid voxel network for lidar based 3d object detection. In: Proceedings of the IEEE/CVF conference on computer vision and pattern recognition. pp. 1631–1640 (2020)
48. Yin, J., Shen, J., Guan, C., Zhou, D., Yang, R.: Lidar-based online 3d video object detection with graph-based message passing and spatiotemporal transformer attention. In: Proceedings of the IEEE/CVF Conference on Computer Vision and Pattern Recognition. pp. 11495–11504 (2020)
49. Yin, T., Zhou, X., Krahenbuhl, P.: Center-based 3d object detection and tracking. In: Proceedings of the IEEE/CVF Conference on Computer Vision and Pattern Recognition. pp. 11784–11793 (2021)
50. Yoo, J.H., Kim, Y., Kim, J., Choi, J.W.: 3d-cvf: Generating joint camera and lidar features using cross-view spatial feature fusion for 3d object detection. In: European Conference on Computer Vision. pp. 720–736. Springer (2020)
51. Zheng, W., Tang, W., Chen, S., Jiang, L., Fu, C.W.: Cia-ssd: Confident iou-aware single-stage object detector from point cloud. In: AAAI (2021)

52. Zheng, W., Tang, W., Jiang, L., Fu, C.W.: Se-ssd: Self-ensembling single-stage object detector from point cloud. In: Proceedings of the IEEE/CVF Conference on Computer Vision and Pattern Recognition. pp. 14494–14503 (2021)
53. Zheng, Z., Wang, P., Liu, W., Li, J., Ye, R., Ren, D.: Distance-iou loss: Faster and better learning for bounding box regression. In: Proceedings of the AAAI Conference on Artificial Intelligence. vol. 34, pp. 12993–13000 (2020)
54. Zhou, Y., Tuzel, O.: Voxelnet: End-to-end learning for point cloud based 3d object detection. In: Proceedings of the IEEE conference on computer vision and pattern recognition. pp. 4490–4499 (2018)
55. Zhu, B., Jiang, Z., Zhou, X., Li, Z., Yu, G.: Class-balanced grouping and sampling for point cloud 3d object detection. arXiv preprint arXiv:1908.09492 (2019)
56. Zhu, X., Zhou, H., Wang, T., Hong, F., Li, W., Ma, Y., Li, H., Yang, R., Lin, D.: Cylindrical and asymmetrical 3d convolution networks for lidar-based perception. IEEE Transactions on Pattern Analysis and Machine Intelligence (2021)